Journal of Fluids and Structures 112 (2022) 103580

Contents lists available at ScienceDirect

Journal of Fluids and Structures

journal homepage: www.elsevier.com/locate/jfs

Passive control of 3D adaptive shock control bumps using a sealed cavity

Michela Gramola [*,1], Paul J.K. Bruce [2], Matthew Santer [3]

Department of Aeronautics, Imperial College London, SW7 2AZ, UK

ARTICLE INFO

Article history:
Received 8 February 2021
Received in revised form 10 December 2021
Accepted 18 April 2022
Available online 25 May 2022

Keywords:
Fluid structure interaction
Adaptive shock control bumps
Flow control
Photogrammetry
Pressure sensitive paint
Cavity pressure

ABSTRACT

This paper presents a Fluid–Structure-Interaction study of a novel passive adaptive shock control bump concept. A flexible plate, clamped on all sides and placed above a sealed cavity, was tested beneath a Mach 1.4 normal shock in the Imperial College London supersonic wind tunnel. The plate was actuated into the shape of a 3D shock control bump by passively controlling the cavity pressure through an array of breather holes. Preliminary experiments were performed with active control of cavity pressure (via a vacuum tank) at Mach 1.4 and 2 to illustrate the potential of this concept. Full-field surface measurement techniques, namely photogrammetry and pressure sensitive paint, were employed in addition to static pressure tappings and schlieren photography. Results confirmed that cavity pressure plays a key role in determining the aerostructural behaviour of the flexible plate. In addition, it was found that carefully placed breather holes allowed the plate to deform into a 3D shock control bump when a shock was on the flexible region and remain flat otherwise. This shows significant potential for improving the off-design behaviour of adaptive shock control bumps.

1. Introduction

Shock control bumps (SCBs) are a flow control mechanism with potential for application to improve the performance of transonic aerofoils. When placed on the suction surface of transonic wings, in the vicinity of the normal shock wave, SCBs bifurcate the normal shock to form a λ-shock structure, such that the supersonic flow is re-compressed by a more efficient system of oblique shocks. While drag reduction and shock stabilisation have been reported on-design, the high sensitivity of SCB performance to flow conditions and the consequent performance deterioration off-design are well known (Bruce and Colliss, 2015; Dargel and Thiede, 2002; Nübler et al., 2012; Babinsky and Harvey, 2011; Stanewsky et al., 2002). In particular, severe flow re-acceleration was reported around the bump crest, associated with the local surface curvature, when the position of the normal shock with respect to the bump crest was sub-optimal. Hence the potential of adaptability to extend the operational envelope over which SCBs are beneficial: by geometric modifications, adaptive SCBs can minimise the off-design performance penalties associated with rigid bumps, without compromising their on-design drag-reducing capabilities.

* Corresponding author.
E-mail address: michela.gramola14@imperial.ac.uk (M. Gramola).
1 Research Associate, Department of Aeronautics, Imperial College London.
2 Reader in High Speed Aerodynamics, Department of Aeronautics, Imperial College London.
3 Reader in Aerospace Structures, Department of Aeronautics, Imperial College London.

https://doi.org/10.1016/j.jfluidstructs.2022.103580

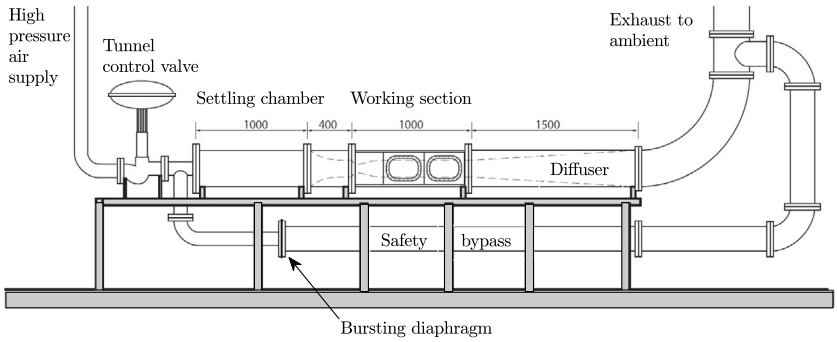

Fig. 1. Schematic diagram of the Imperial College London supersonic wind tunnel (Threadgill and Bruce, 2020).

Extensive research on 2D adaptive SCBs has been carried out at Imperial College London in recent years (Jinks et al., 2018; Gramola et al., 2018, 2020). These experimental studies have shown the importance of employing some actuation mechanism to facilitate the deformation of the flexible plate into a drag-reducing SCB at wind-on conditions and completely retract off-design, such that an unaffected normal shock can be maintained above the undeployed bump. Successful deformations were obtained with linear actuators, but previous work has also identified the pressure in the cavity underneath the flexible plate as a powerful actuation mechanism (Jinks et al., 2018). The impact of the pressure underneath a flexible plate on its dynamic behaviour when subject to the pressure loading of a shock wave has also been highlighted by Visbal (2014). However, literature is still lacking a systematic study of the effect of cavity pressure on the behaviour of a thin flexible plate placed beneath a shock wave.

Some recent studies on rigid SCBs have investigated the potential of employing arrays of locally-optimised 3D SCBs to suit the performance requirements of different regions of real swept wings (Jones and Jarrett, 2018). However, little is known about the aerostructural behaviour of 3D adaptive SCBs and whether the trends observed for 2D adaptive SCBs would also be valid in 3D. In addition, previous work has highlighted the challenges of reaching the required 3D bump heights within the elastic range with a limited number of discrete actuation points (Rhodes and Santer, 2011), suggesting the need for alternative actuation methods.

A common aim of the experimental work on Shock Wave/Boundary Layer Interactions (SBLIs) on flexible plates in recent years has been to fully characterise the coupled aerodynamic and structural response. This has necessitated full-field non-intrusive experimental techniques to allow simultaneous pressure and surface measurements, the latter often achieved through Digital Image Correlation (DIC) (Beberniss et al., 2012; Daub et al., 2015; Peltier et al., 2019; Spottswood et al., 2019).

This paper presents a Fluid–Structure-Interaction (FSI) study of a novel 3D SCB concept. A flexible plate, clamped on all sides and placed above a sealed cavity, was tested at Mach 1.4 and passively actuated into a 3D SCB shape by controlling the cavity pressure through an array of breather holes. Preliminary experiments are also presented with active control of cavity pressure by means of a vacuum tank. Full-field surface measurement techniques were employed to capture 3D effects.

2. Experimental setup

2.1. Imperial college London supersonic wind tunnel

Experiments were carried out in the Imperial College London supersonic wind tunnel, a schematic diagram of which is shown in Fig. 1. It is a blow-down facility that allows a maximum run time of approximately 1 min. The working section has a constant square cross section with height = width = 150 mm and length = 727 mm. The nozzle blocks can be interchanged to generate supersonic flow with Mach number 1.4 or 2 in the working section. Tests were performed with a Mach 1.4 normal shock and a Mach 2 oblique shock produced by a 10° shock generator.

Typical freestream and boundary layer parameters for the wind tunnel were calculated by Threadgill and Bruce (2015) for two configurations (an incident oblique shock produced by an 8° shock generator and a normal shock) and are reported in Tables 1 and 2. In the absence of a shock, streamwise changes in properties in the working section are small and, in most cases, can be considered negligible. The unit Reynolds number in the tunnel is approximately 2.7×10^7 m^{-1}.

A LabVIEW script, including a Proportional–Integral–Derivative (PID) controller, was used to run the tunnel. It monitored the pressure in the settling chamber and adjusted the aperture of a pneumatic valve to keep the tunnel stagnation pressure at the requested value, which was typically achieved within ±0.3%. These small variations in stagnation pressure were observed to occur at a frequency of the order of 1 Hz and gave rise to oscillations of the normal shock in the wind tunnel working section.

Table 1
Freestream parameters in the Imperial College supersonic wind tunnel working section from Threadgill and Bruce (2015). The subscript e indicates the conditions at the nozzle exit.

Configuration	P_0 [kPa]	M_e	u_e [m/s]	T_0 [K]	u'/u_e [%]	v'/u_e [%]
Shock reflection	210	1.97	519	307	1.4	0.8
Normal shock	128	1.38	389	274	2.1	1.3

Table 2
Compressible boundary layer parameters in the Imperial College supersonic wind tunnel working section (incompressible values in parentheses) from Threadgill and Bruce (2015).

Configuration	δ_0 [mm]	δ^* [mm]	θ [mm]	H	Re_θ	C_f	u_τ [m/s]
Shock reflection	5.87	1.09 (0.59)	0.73 (0.46)	1.49 (1.28)	19 200	0.00226	22.8
Normal shock	4.73	0.91 (0.61)	0.61 (0.46)	1.49 (1.33)	13 200	0.00234	16.3

2.2. Adaptive SCB design

Fig. 2 shows sketches of the models installed in the wind tunnel and Fig. 3 a photograph of the thin plate used in the normal shock experiments. For all the tests described in this paper, the model was a 0.6 mm-thick flexible plate, which was milled out by CNC machine from a nominally rigid 2 mm-thick plate, made of aluminium alloy Al-7075-T6, to ensure built-in boundary conditions on all sides. The flexible region was 100 mm wide, and its length $L_1 = 200$ mm for the oblique shock tests. This was reduced to $L_2 = 150$ mm for the normal shock tests to enable displacement and pressure measurements of the entire flexible region to be made, given the limited field of view of the cameras. Dimensions in this paper are normalised by either $L_1 = 200$ mm or $L_2 = 150$ mm, depending on the experiments described. The plate was designed such that only the thinner (0.6 mm) region would (elastically) deform during experiments due to the pressure differential across it. However, experiments revealed that the nominally rigid (2 mm-thick) portion of the plate also deflected slightly under the pressure loading, with peak displacements of $y/L_1 = \pm 0.005$ at the leading and trailing edges of the flexible region (during experiments with a Mach 2 oblique shock).

2.3. Cavity

Fig. 4 shows a schematic diagram of the cavity system. During experiments, the thin plate was bolted onto a thicker floor piece, and the other side of the cavity, of total volume 1.2 L, sealed with a sealing plate. A cavity gasket was inserted between the sealing plate and the wind tunnel frame and vacuum grease, wax and hot glue were applied to improve the seal. The sealing plate was connected to a 150 L vacuum tank and a vacuum pump was used to evacuate the tank, achieving a minimum tank pressure below 10 kPa.

The pressure below the flexible plate, as well as above, is known to strongly affect its aerostructural behaviour (Visbal, 2014). To investigate this further, the cavity pressure was carefully controlled and monitored during the experiments described in this paper. Active control was exerted through a manually-operated ball valve between the sealing plate and the vacuum tank, which had been previously evacuated to the desired pressure by means of a vacuum pump. In some experiments, passive control of the cavity pressure was achieved through an array of six breather holes with diameter 1.7 mm, placed at a streamwise location of $x/L = 0.73$, as shown in Fig. 3. The purpose of the breather holes was to passively actuate the flexible plate into the shape of a 3D SCB at certain predetermined flow conditions, by allowing some airflow between the cavity and the working section. For this reason, during the experiments with breather holes the ball valve was kept closed to isolate the cavity from the vacuum tank. In both cases, the pressure in the cavity was measured at a streamwise location of $x/L_1 = 0.375$ or $x/L_2 = 0.5$ and preliminary experiments revealed that pressure was uniform within the cavity.

3. Experimental methodology

3.1. Schlieren photography

A Z-type schlieren arrangement was used with a horizontal knife edge configuration. Light from a Thorlabs MCWHL5 LED point source with 800 mW power and 1 mm pinhole diameter was reflected on two 200 mm-diameter concave mirrors with focal length 1200 mm. Schlieren videos were recorded at 100 Hz, with resolution of 1800 × 1552 pixels and exposure time of 30 μs. A typical schlieren image from experiments with a Mach 1.4 normal shock and cavity pressure $P_c/P_0 = 0.76$ is shown in Fig. 5. Labels indicate the location of the flexible plate, the boundary layers, Mach waves and the bifurcated shock structure. The main normal shock is bifurcated because the surface curvature at the front of the flexible plate generates compression waves that coalesce into an oblique shock, leading to a lambda shape, typical of transonic flow above an SCB, with the normal shock, front and rear legs intersecting at the triple point (Gramola et al., 2018). An

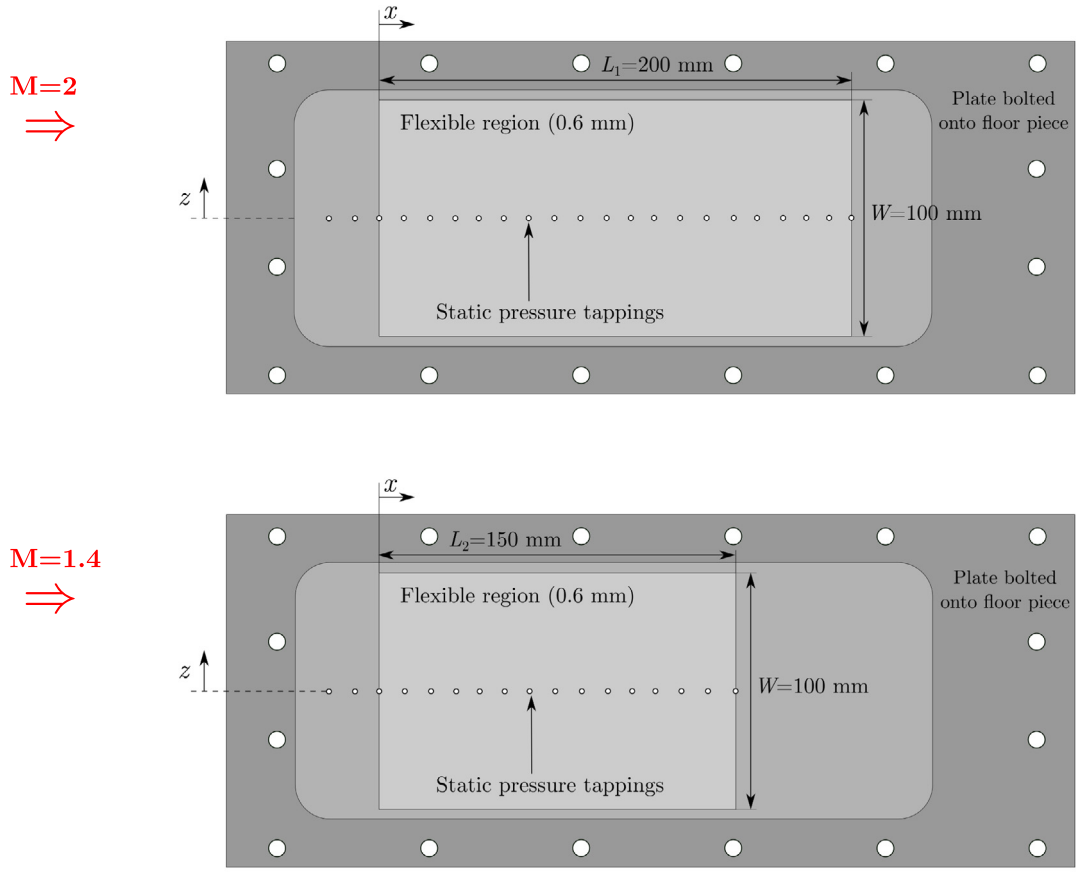

Fig. 2. Sketches of the 3D adaptive SCB (top view). Top plate used for the oblique shock experiments ($M = 2$). Bottom plate used for the normal shock experiments ($M = 1.4$). Dark grey: areas where the plate is bolted onto the floor piece, mid grey: 2 mm-thick region, light grey: flexible (0.6 mm-thick) region.

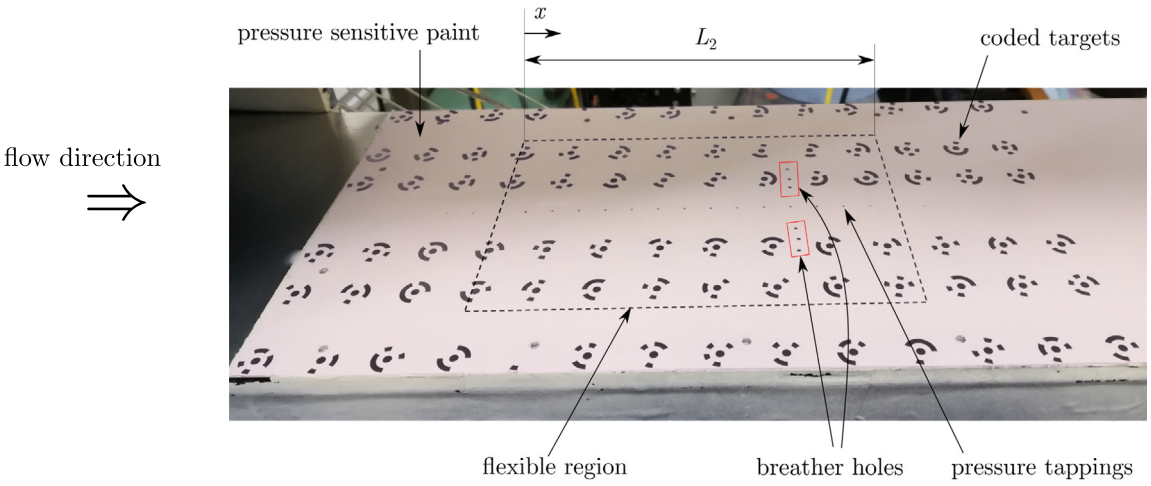

Fig. 3. Photograph of the thin plate used for the normal shock experiments ($L_2 = 150$ mm) with key features indicated.

additional bifurcation of the rear leg can be observed close to the flexible surface (secondary lambda) due to the local SBLI there.

It should be noted that an assessment of shock unsteadiness is beyond the scope of this work and will not be discussed in this paper.

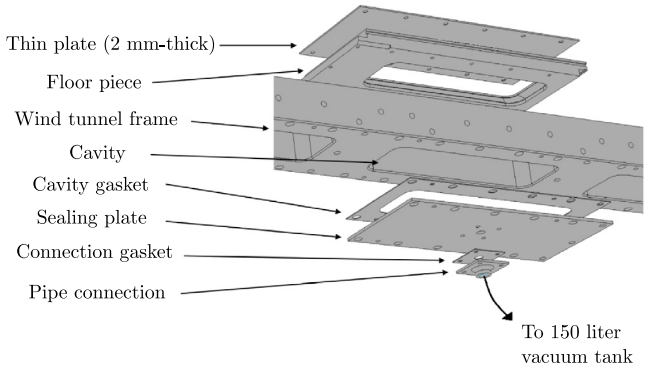

Fig. 4. Schematic diagram showing the cavity system (Ravichandran et al., 2020).

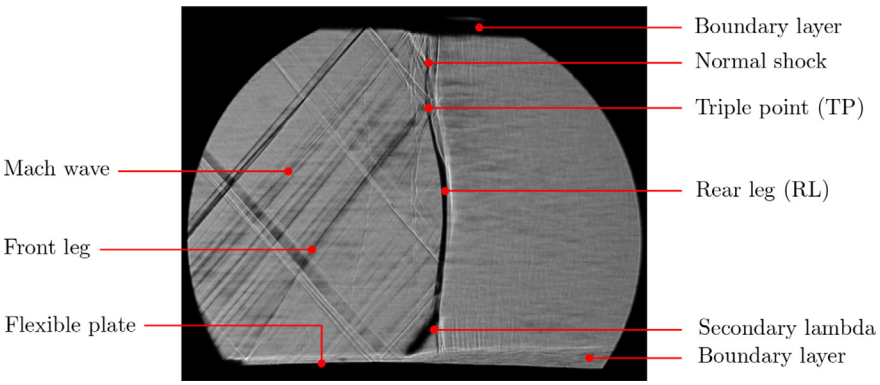

Fig. 5. Typical schlieren image of a bifurcated normal shock above a 3D flexible plate with key features indicated. $P_c/P_0 = 0.76$, $M = 1.4$, $P_0 \approx 130$ kPa.

3.2. Photogrammetry

Accurate measurement of the plate deformation during experiments was achieved by point-tracking photogrammetry (Gramola et al., 2019). As shown in Fig. 6(a), four Phantom high-speed cameras were placed around the working section, where the flexible surface was patterned with 80 vinyl-cut coded targets (with thickness 20 μm) at regular spacing (Fig. 3). Videos were recorded at 100 Hz, and the commercial photogrammetry software photoModeler by EOS Motion (PhotoModeler, 2018) was used to generate a 3D model of the surface. The RMS error calculated for this setup is 30 μm (Gramola et al., 2019), which is considered negligible for the experiments presented in this paper.

3.3. Pressure measurements

Static pressure measurements on the side of the nozzle and along the centreline of the flexible plate were obtained through 32 static pressure tappings, with internal hole diameter 0.5 mm (Fig. 3). Meier (1977) suggested that errors in static pressure measurement can be minimised with small diameter pressure tappings, and the ones used should give negligible errors. Rubber tubes connected each tapping to a remote pressure transducer, contained within two NetScanner 9116 Pressure Scanner modules and sampling at 100 Hz. The stagnation pressure was measured with a static pressure tapping placed in the settling chamber, using an empirical correction factor to account for the non-zero flow velocity. Pressure was sampled for the whole duration of the experiments and recording was triggered within the main LabVIEW script at the beginning of each test.

The uncertainty associated with the pressure reading is ±0.15%, according to the specifications of the transducers, which means that the measurement error should be within ±200 Pa. Considering that pressure waves travel at $M = 1$, with an average length of the tubing system of 1 m the response time of the pressure system is approximately 3 ms, which gives confidence in the temporal accuracy of the measurements taken at 100 Hz. Furthermore, the quoted maximum sampling frequency of the Netscanner 9116 is 500 Hz.

Table 3
Specifications of the binary UniCoat Pressure Sensitive Paint from ISSI (2019).

Pressure sensitivity	0.5%/kPa
Temperature sensitivity	0.9%/K
Response time	0.750 s
Excitation wavelength	380–520 nm
Emission wavelength	500–750 nm

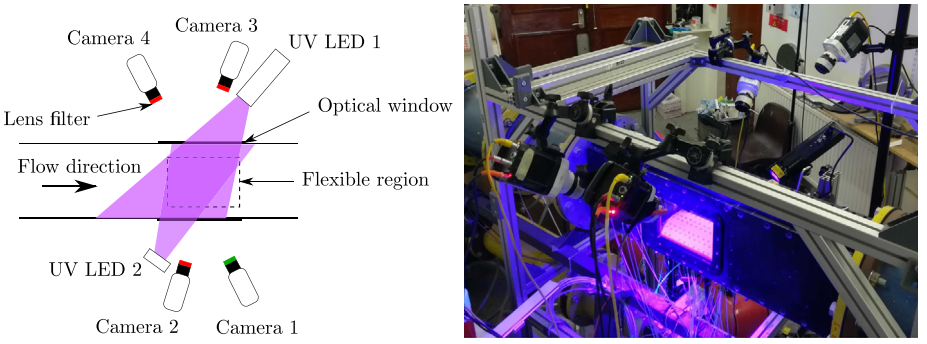

(a) Schematic diagram (b) Photograph

Fig. 6. Experimental setup for simultaneous PSP and photogrammetry measurements. (For interpretation of the references to colour in this figure legend, the reader is referred to the web version of this article.)

In addition, Pressure Sensitive Paint (PSP) was used during the Mach 1.4 normal shock experiments to capture the 3D pressure field on the flexible surface. The binary UniCoat paint from Innovative Scientific Solutions Incorporated (ISSI) (ISSI, 2019) was chosen for its practical aerosol application and good pressure sensitivity (Table 3). However, the low signal-to-noise ratio for the pressure-insensitive channel meant that the binary PSP was effectively employed as a single-component paint, with peak emission at 650 nm. A set of 100 wind-off frames, taken at the beginning of the test, was averaged to minimise the influence of digital camera noise.

Fig. 6 shows a schematic diagram and a photograph of the PSP setup. Two continuously operating (DC) UV LED arrays with peak wavelength 400 nm and combined optical power 7 W were placed on either side of the working section to provide uniform, stable illumination during experiments. The same videos, recorded with the four high-speed cameras, were used for the photogrammetry and PSP post-processing, provided that the cameras were equipped with optical filters (long pass optical filters with a cut-on wavelength of 600 nm) to remove the high intensity UV light from the images. From Fig. 6(a) it can be seen that one of the cameras was fitted with a green band-pass filter (490–570 nm). This was used to isolate the pressure-insensitive component of the binary paint, which was however not employed in the final analysis. The videos were recorded at 100 Hz with an exposure time of 10 ms.

Photogrammetry targets were placed on top of the pressure sensitive paint (as shown in Fig. 3). Image registration was performed in MATLAB and involved using a 'local weighted mean' second-order polynomial to map the wind-on images of the deflected flexible plate to the corresponding wind-off coordinates based on the detected location of the coded targets in the two cases. Following image registration, the ratio of pixel intensities between wind-on and wind-off conditions was calculated.

A study was done to investigate the temperature sensitivity of PSP for this experimental setup (Gramola et al., 2021). Diagnostic experiments were performed and a heat transfer solver was written in MATLAB to predict the thermal behaviour of the plate. While the key findings are summarised in this section, details of the analysis are beyond the scope of this paper and are described in Gramola et al. (2021). The plate temperature was found to decrease with time as a result of the drop in tunnel stagnation temperature and in-plate conductive heat transfer. In addition, step changes in model thickness led to temperature non-uniformities across the plate, which worsened with time. Variations in adiabatic wall temperature across the plate due to shocks, compression waves and expansion fans further contributed to local temperature changes. Therefore, the PSP in-situ calibration was only accurate along the plate centreline, where the static pressure tappings were located. Temperature-dependent calibration coefficients ($A(T)$ and $B(T)$) were determined and applied to the regions of the plate with different temperatures (as estimated from the heat transfer solver) to account for temperature gradients. Finally, the relationship between image intensity at a given pixel (I) and surface pressure (P) was given by the Stern–Volmer equation

$$\frac{I_{\mathrm{REF}}}{I} = A(T) + B(T)\,\frac{P}{P_{\mathrm{REF}}}, \tag{1}$$

with

$$A(T) = 0.0020\,(T_{0,\mathrm{start}} - T) + 0.55 \tag{2}$$

and

$$B(T) = -0.016\,(T_{0,\text{start}} - T) + 0.45. \tag{3}$$

$T_{0,\text{start}} = 285$ K is the initial tunnel stagnation temperature and T the local plate temperature estimated from the heat transfer solver.

4. Results

Throughout this paper, shock position is indicated by either the impingement point of the shock on the flexible surface (x_{RL}) or by the triple point (x_{TP}), based on which part of the shock is of interest. The rear leg position is defined as the point where $P/P_0 = 0.528$ along the centreline ($z/L_1 = z/L_2 = 0$) for results from the pressure tappings, and between $z/L_2 = -0.02$ and -0.04 (taking a spanwise average over 10 pixels) for the PSP. The average PSP profile was further smoothed by calculating a moving average with window size 70 pixels (≈21 mm). The triple point position was detected from schlieren images, as per (Gramola et al., 2018).

4.1. Active control of cavity pressure

Active control of cavity pressure was achieved by evacuating the 150 L vacuum tank to the desired pressure before the experiment and opening the valve at the bottom of the cavity during the test. Small leaks from the laboratory into the cavity meant that the cavity pressure increased slightly over the course of an experiment and data was discarded if P_c did not lie within ±2 kPa of the target value. In the next sections, experiments with active control of cavity pressure are discussed with both a Mach 2 oblique shock and a Mach 1.4 normal shock.

4.1.1. Mach 2 oblique shock

Fig. 7 shows 3D surface deformations from photogrammetry and corresponding schlieren images for the case of a Mach 2 oblique shock impinging on the flexible surface with three different values of cavity pressure ($P_c/P_0 = 0.5$, 0.2 and 0.05, with $P_0 = 200$ kPa). The oblique shock was generated by a 10° shock generator and impinges on the surface at $x_{\text{RL}}/L_1 = 0.44$.

Fig. 7 shows that the aerostructural behaviour of the flexible surface is significantly influenced by the pressure in the cavity. For the highest cavity pressure ($P_c/P_0 = 0.5$), the plate deflects significantly into the flow, leading to a deformed shape that resembles a typical 3D SCB, composed of a ramp, followed by a crest region and a tail (Fig. 7(a)). The high surface curvature at the leading edge of the plate generates an oblique shock (Fig. 7(b)). The intermediate cavity pressure tested ($P_c/P_0 = 0.2$) leads to a more complex plate shape, with positive deformation upstream of the shock and negative deformation downstream of the shock (Fig. 7(c)). As a result, a weaker oblique shock is generated at the front of the flexible plate (Fig. 7(d)). For $P_c/P_0 = 0.05$, the very low cavity pressure causes the surface to exhibit a negative deflection, away from the flow (Fig. 7(e)). The positive curvature at the front of the flexible plate generates expansion waves (Fig. 7(f)).

Figs. 7(a), 7(c) and 7(e) show that the distorted shapes are highly 3D, which is expected as the flexible plate is constrained on all sides. Therefore, the flow structures above the plate necessarily show spanwise variations, with the strongest shock waves and expansions around the centreline ($z/L_1 = 0$). However, it is difficult to observe these differences from schlieren images (Figs. 7(b), 7(d) and 7(f)), as schlieren provides a spanwise-averaged visualisation and because the coded targets attached to the wind tunnel floor (with thickness 20 μm) generate Mach waves. For the purpose of clarity, when comparing surface deformations and pressure profiles, centreline values will be shown, but the 3D nature of the problem should be kept in mind and will be revisited in Section 4.2.3.

Fig. 8(a) shows the average centreline plate displacement at wind-on conditions for a range of cavity pressures between $P_c/P_0 = 0.05-0.5$. It can be seen that, as expected, as the cavity pressure is increased, the plate deforms from a negatively deflected shape ($P_c/P_0 \leq 0.15$) to a positively deflected shape ($P_c/P_0 \geq 0.25$). However, Fig. 8(a) also shows the interesting sinusoidal shape for $P_c/P_0 = 0.20$. With respect to the boundary layer displacement thickness ahead of the shock, the maximum centreline place displacements are $y/\delta^* = 2.9$ and $y/\delta^* = 2.1$ in the positive and negative y-direction, respectively.

Fig. 8(b), which shows centreline pressure distributions, can help explain the differences between the profiles in Fig. 8(a). For all the cavity pressures tested, a strong pressure rise is detected at $x/L_1 \approx 0.4$, followed by a drop at $x/L_1 \approx 0.6$, as a result of the oblique shock and expansion fan originating from the shock generator (SG). While this trend can also be observed for the solid flat plate case (black asterisks in Fig. 8(b)), some subtle differences associated with plate deformation are most visible for $x/L_1 < 0.3$. As expected, flow compression is seen to occur for the cases with negative plate curvature (and positive deflection) and expansion for those with positive curvature (and negative deflection). Defining $\Delta P = (P_c - P_{\text{freestream}})/P_0$, if ΔP is consistently positive or negative, the plate will deform in either the positive or the negative y-direction, respectively. However, if ΔP changes sign along the flexible plate, it could result in a sinusoidal deformed shape, as for $P_c/P_0 = 0.20$: the plate exhibits a positive displacement for $0 < x/L_1 < 0.5$, and a negative displacement for $0.5 < x/L_1 < 1$, with an inflection point around $x/L_1 = 0.5$, where $\Delta P \approx 0$.

Figs. 7 and 8(a) show that the constraints of zero curvature and vertical displacement at the boundaries of the flexible plate ($x/L_1 = 0$ and 1) are not fully enforced. It should also be noted that, due to the limited field of view, it was not possible to obtain the 3D coordinates of the most downstream row of targets (at $x/L_1 = 1$). Therefore, a new wind tunnel model with a shorter flexible region (as per Fig. 2) was used in the Mach 1.4 experiments.

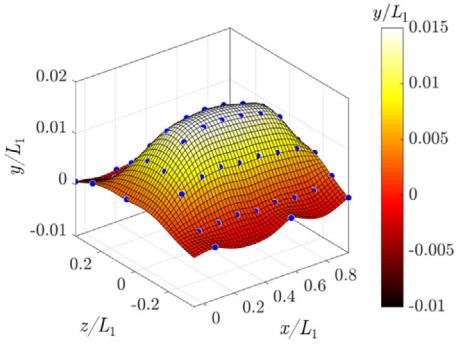

(a) Plate shape for $P_c/P_0 = 0.5$.

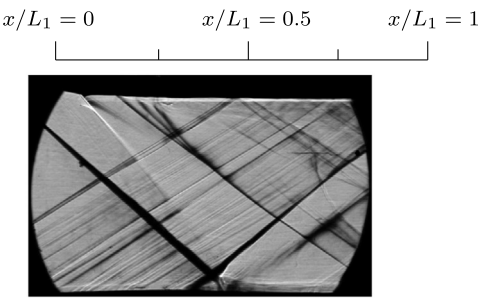

(b) Schlieren image for $P_c/P_0 = 0.5$.

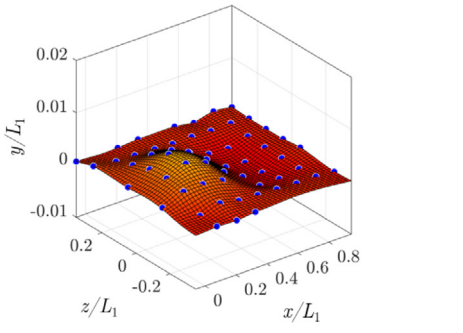

(c) Plate shape for $P_c/P_0 = 0.2$.

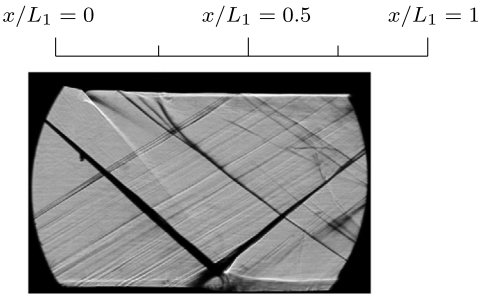

(d) Schlieren image for $P_c/P_0 = 0.2$.

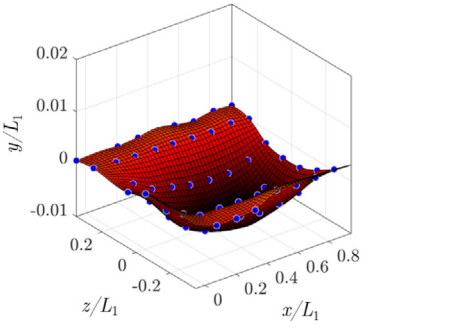

(e) Plate shape for $P_c/P_0 = 0.05$.

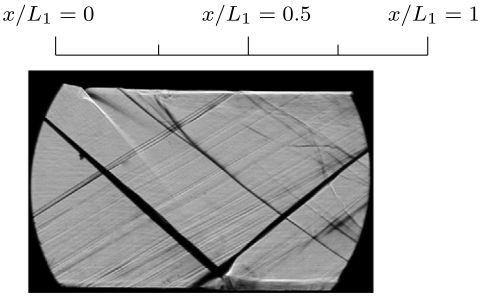

(f) Schlieren image for $P_c/P_0 = 0.05$.

Fig. 7. 3D plate shapes and corresponding schlieren images for three cavity pressures with an oblique shock at $x_{RL}/L_1 = 0.44$. $M = 2$, $P_0 = 200$ kPa.

4.1.2. Mach 1.4 normal shock

Unlike the oblique shock experiments presented in Section 4.1.1, tests at Mach 1.4 involve a normal shock that experiences small oscillations in streamwise position as a result of slight variations in tunnel stagnation pressure. Therefore, for a given cavity pressure, a range of plate shapes and pressure distributions was observed due to variations in pressure differential across the plate throughout a test. Hence, in this section, results are presented as a function of cavity pressure and triple point position.

Average plate shape. The average plate shape (represented by the centreline displacement) as a function of triple point position was calculated based on measured displacements at ten discrete streamwise positions, where the coded targets were applied. From the lines of best fit through these points, average plate profiles over a range of triple point positions were reconstructed. Fig. 9 shows the variation of average plate shape for a range of triple point positions and five different cavity pressures (with $P_0 \approx 130$ kPa). For the highest cavity pressures ($P_c/P_0 = 0.76$ and 0.61) the plate deforms into the flow due to the positive ΔP and it assumes the shape of a 3D SCB. For the intermediate value of $P_c/P_0 = 0.45$, the plate assumes a sinusoidal shape, due to ΔP changing sign along the plate. For the lowest cavity pressures ($P_c/P_0 = 0.15$ and

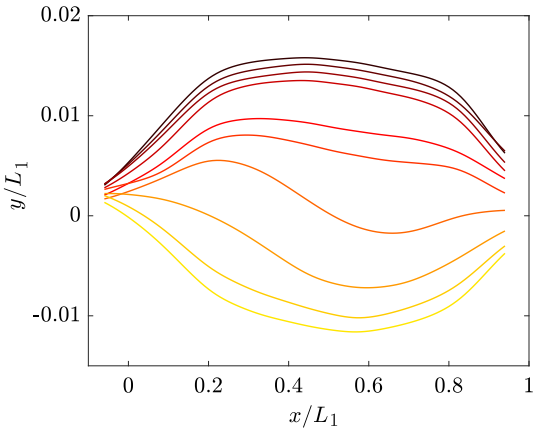

(a) Centreline plate displacement.

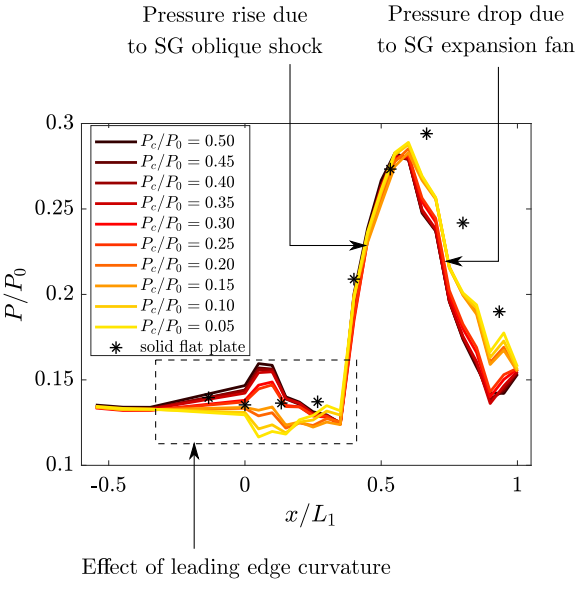

(b) Centreline pressure distribution.

Fig. 8. Centreline plate displacement and corresponding pressure distribution for a Mach 2 oblique shock with $x_{RL}/L_1 = 0.4$, cavity pressures between $P_c/P_0 = 0.05-0.5$ and $P_0 = 200$ kPa. The baseline pressure profile for a solid flat plate is added for comparison. The same legend applies to both plots.

0.30), the plate exhibits negative deformations as $\Delta P < 0$. With respect to the boundary layer displacement thickness ahead of the normal shock, the maximum plate displacement is $y/\delta^* = 2.9$ and $y/\delta^* = 3.3$ in the positive and negative vertical direction.

The results in Fig. 9 are consistent with those in Fig. 8(a). However, Fig. 9 shows another layer of complexity compared with Fig. 8(a): the aerostructural coupling driven by the normal shock moving back and forth along the thin plate leads to significant changes in plate shape throughout an experiment. The greatest variation is observed for the intermediate cavity pressure $P_c/P_0 = 0.45$ (Fig. 9(c)), where the small pressure differential across the plate means that minor changes in shock position have a strong impact on the surface deformation.

Stagnation pressure loss and shock stability. To provide some context, stability of a normal shock in a parallel duct (representing the wind tunnel working section) is discussed in the Appendix. It is shown that, for a blow-down wind tunnel that exhausts to atmosphere (which fixes the overall stagnation pressure losses in the working section for a given inlet stagnation pressure), P_0/P_e can be regarded as an indication of the stagnation pressure loss associated with the shock structure. Therefore, for a given rear leg and triple point position, a lower value of P_0/P_e suggests lower losses.

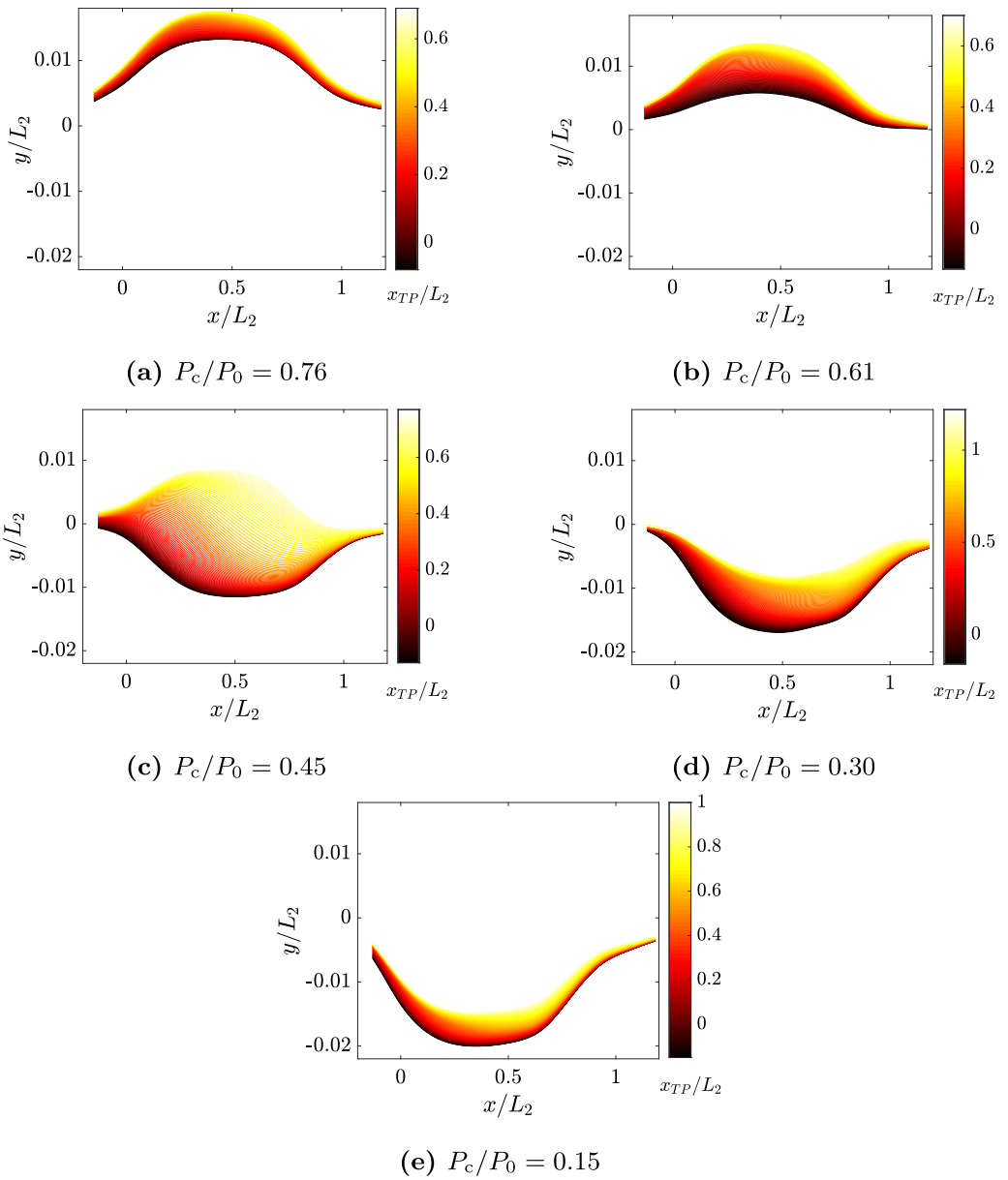

Fig. 9. Average centreline plate shape as a function of triple point position for five different cavity pressures. $M = 1.4$, $P_0 \approx 130$ kPa.

Fig. 10 shows plots of the ratio of inlet to exit tunnel stagnation pressure (P_0/P_e) against normalised rear leg position (x_{TP}/L_2) for the five cavity pressures tested, compared with the baseline case of a solid flat plate. It should be noted that the exit pressure P_e was constant during a test and equal to the atmospheric pressure. Therefore, the variation in P_0/P_e was provided by the small changes in P_0 associated with the tunnel PID controller, as discussed in Section 2.1. Such small P_0 variation was sufficient to cause the position of the normal shock to vary slowly in the wind tunnel working section. The rear leg position is determined from the pressure readings on the flexible surface, and is defined as the point at which $P/P_0 = 0.528$, nominally corresponding to $M = 1$ in the absence of any losses. Statistical binning of the instantaneous data is employed to calculate representative mean values with bin size $\Delta(x_{RL}/L_2) = 0.05$.

Considering the profiles in Fig. 10, it can be concluded that the loss-reducing potential of the deformed flexible plate is strongly dependent on cavity pressure. For $P_c/P_0 = 0.76$ and 0.61 (which correspond to the plate shapes in Figs. 9(a) and 9(b) respectively) the positively deflected plate reduces stagnation pressure losses compared with the solid flat plate case. This is consistent with previous research on SCBs (Gramola et al., 2018, 2020; Bruce and Colliss, 2015): as shown in Fig. 11(a), the surface curvature at the leading edge of the flexible surface bifurcates the normal shock into a λ-shock. The resultant pressure rise is obtained through a more efficient oblique shock (front leg), followed by a weaker normal

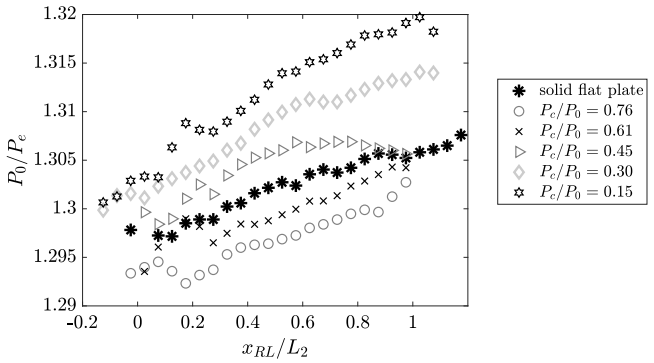

Fig. 10. Plots of stagnation pressure ratio as a function of rear leg position for the flexible plate with different cavity pressures and the baseline case of a solid flat plate. $M = 1.4$, $P_0 \approx 130$ kPa.

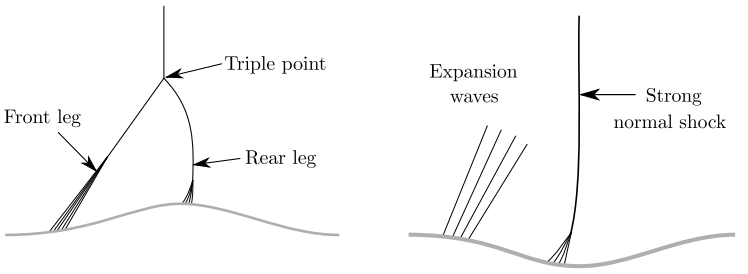

(a) Plate deformed into the flow. **(b)** Plate deformed away from the flow.

Fig. 11. Schematic diagram of the flow structure above the flexible plate with different shapes.

shock (rear leg), leading to a stagnation pressure saving for most shock positions. However, for upstream shock positions ($x_{RL}/L_2 \approx 0.1$), re-acceleration of the subsonic post-shock flow has been observed, and for downstream shock positions ($x_{RL}/L_2 \approx 0.9$) supersonic re-acceleration of the flow between the front and rear legs and consequent increase in the strength of the normal shock are known to happen (Gramola et al., 2018). These phenomena imply that an increase in stagnation pressure losses is expected for shock positions close to the leading and trailing edges of the flexible region, and this is consistent with the profiles for $P_c/P_0 = 0.76$ and $P_c/P_0 = 0.61$ in Fig. 10, which can be seen to approach the baseline for $x_{RL}/L_2 \approx 0$ and $x_{RL}/L_2 \approx 1$.

For $P_c/P_0 = 0.30$ and 0.15 (plate profiles in Figs. 9(d) and 9(e)), the concave plate shape means that an expansion fan is generated at the leading edge of the flexible region (Fig. 11(b)). Flow expansion leads to a stronger normal shock, which is associated with increased losses. This is confirmed by the profiles in Fig. 10, which lie above those for the solid flat plate.

The wide range of plate shapes observed for $P_c/P_0 = 0.45$ (as per Fig. 9(c)) has an interesting effect on shock stability. Fig. 9(c) shows that, for the more upstream shock positions, the plate is deflected away from the flow, while, as the shock moves downstream and the flexible surface is exposed to a larger supersonic low-pressure region, an SCB-like shape appears. As explained in the previous paragraphs, convex and concave plate shapes are associated with opposing trends as regards stagnation pressure losses: specifically a reduction for the former and an increase for the latter. Therefore, the shock stability line for $P_c/P_0 = 0.45$ in Fig. 10 is close to that for $P_c/P_0 = 0.30$ for upstream shocks, but diverges from $x_{RL}/L_2 \approx 0.4$ and approaches the baseline as the flexible plate deforms into the flow.

From the results in Fig. 10 it can be concluded that the flexible plates with the higher values of cavity pressure (i.e. 3D SCBs) lead to a reduction in stagnation pressure losses for all shock positions considered. However, Fig. 10 does not give a clear indication of the off-design behaviour of the SCBs and, as shown in Fig. 20, even beneficial shock control devices are associated with an off-design performance degradation if they are permanently deployed into the flow. Therefore, next section discusses the concept of a passively-controlled 3D SCB that deploys on-design and remains flat off-design.

4.2. Passive control of cavity pressure through breather holes

Section 4.1 has shown that cavity pressure is a powerful actuation mechanism, which has a strong influence on the aerostructural behaviour of the flexible surface. A study was done to explore the feasibility of passively controlling cavity

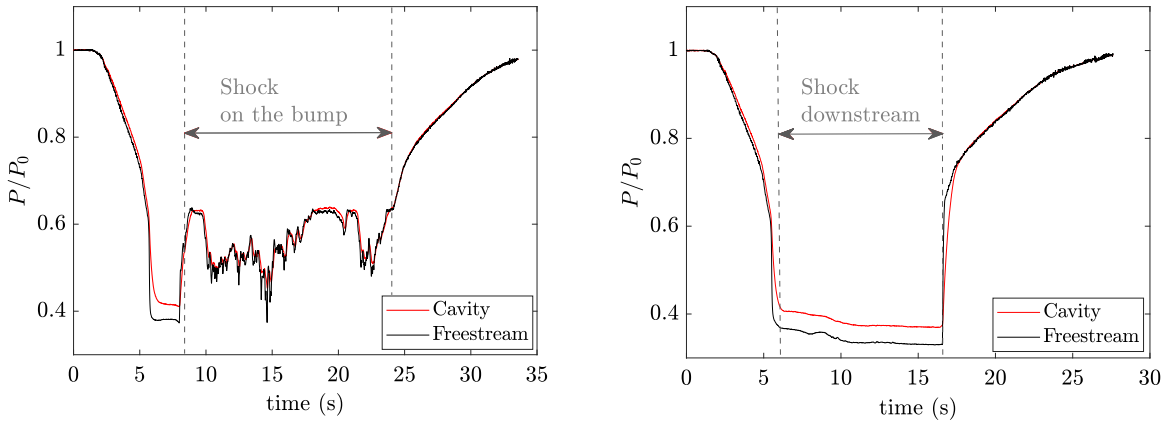

(a) Shock oscillating on the bump. **(b)** Shock downstream of the bump.

Fig. 12. Comparison between cavity and freestream pressure for representative tests with six breather holes located at $x/L_2 \approx 0.73$. $M = 1.4$, $P_0 \approx 130$ kPa.

pressure during experiments through an array of breather holes. They allow a small airflow between the (otherwise sealed) cavity and the working section, such that the pressure in the cavity approaches the pressure in the working section at the location of the breather holes.

Preliminary Mach 2 experiments with a steady oblique shock aided the sizing and placement of the breather holes to ensure positive deformations of the flexible plate into the flow for a range of shock positions and passive deformation of the resulting SCB to accommodate shock motion. Six breather holes with diameter 1.7 mm were added to the plate. This ensures that the mass flow rate through the breather holes is significantly larger than the leakage mass flow rate (i.e. the mass flow rate of air leaking from the laboratory into the cavity and from the cavity into the working section other than through the breather holes) and so achieves high sensitivity of cavity pressure to the freestream pressure above the breather holes, which is determined by shock position.

In addition, the breather holes had to be carefully positioned to ensure that the pressure in the cavity was higher than the average freestream pressure above the plate for all shock positions. For this reason, they were placed on the downstream half of the plate, where the pressure of the post-shock subsonic flow would ensure deformations of the flexible plate into the flow. Finally, the plate shape had to change as a result of shock position to extend the operational envelope over which the SCB is effectively on-design. In particular, the bump crest had to "follow" the normal shock to avoid undesirable flow expansion. A range of breather hole positions were tested and it was found that these requirements could be achieved with six breather holes at $x/L_2 = 0.73$, and within $z/L_2 = \pm 0.2$, as shown in Fig. 3.

It should be noted that all the experiments described in this section were performed at Mach 1.4 and with the cavity isolated from the vacuum chamber.

Fig. 12 shows the comparison between the cavity and freestream pressure, measured at the nozzle exit, during two representative wind tunnel experiments. In Fig. 12(a) the shock is positioned on the bump between 8−24 s, and a good match can be observed between cavity and freestream pressures in this time interval, with an average difference of $\Delta P/P_0 = 0.005$, or 1%. Fig. 12(b) presents results for the case of a shock held downstream of the working section for the entire wind tunnel run. It can be seen that, as the tunnel starts up and the shock is swept downstream, the cavity pressure settles to $P_c/P_0 \approx 0.4$, despite the freestream pressure being lower. In this case, the average pressure difference between 7−16 s is $\Delta P/P_0 = 0.04$, or 12%. A study was made to show that, below $P_c/P_0 \approx 0.4$, the leakage mass flow rate becomes significant and the cavity pressure cannot be reduced further through the passive effect of the breather holes. For the experiments presented in this paper, the cavity pressure is typically $P_c/P_0 = 0.5-0.6$, hence the mass flow through the breather holes is usually significantly larger than the leakage mass flow rate.

Considering Fig. 12, it can be concluded that this experimental setup is appropriate to study 3D adaptive SCBs employing cavity pressure as a passive actuation mechanism, albeit with a pressure difference between the cavity and the freestream for shocks downstream of the bump.

4.2.1. Average plate shape

Fig. 13 shows the average centreline plate shapes as a function of triple point position for $-0.14 < x_{TP}/L_2 < 0.73$, analogous to Fig. 9 for the experiments with active cavity pressure control. At wind off the bump is approximately flat, with some small waviness associated with the installation of the thin plate in the wind tunnel. Likewise, when the shock is upstream of the bump, the pressure on the flexible plate is uniform and equal to the cavity pressure, hence the plate is still in its undeformed configuration. As x_{TP}/L_2 increases (and hence the low-pressure region extends on the flexible plate),

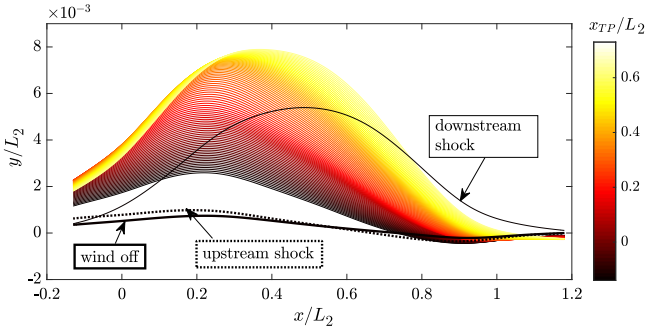

Fig. 13. Average centreline plate shape as a function of triple point position ($-0.14 < x_{TP}/L_2 < 0.73$) for experiments with breather holes. $M = 1.4$, $P_0 \approx 130$ kPa.

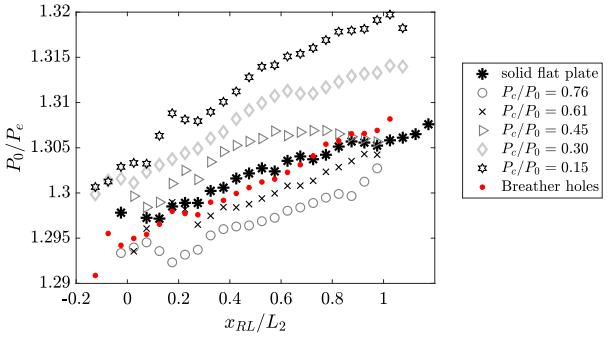

Fig. 14. Shock stability lines for the flexible plate with active (using a vacuum pump) and passive (through breather holes) control of cavity pressure, and the baseline case of a solid flat plate. $M = 1.4$, $P_0 \approx 130$ kPa.

the bump becomes taller and the crest shifts downstream, which is known to be beneficial for extending the operational envelope of adaptive SCBs (Gramola et al., 2020). The maximum displacement corresponds to $y/\delta^* = 1.3$.

Limitations in the experimental setup, namely shock reflection on the top of the wind tunnel for $x_{TP}/L_2 > 0.73$, mean that more downstream triple point positions could not be tested. However, the profile for a shock downstream of the bump (thin black line in Fig. 13) is shorter than that for $x_{TP}/L_2 = 0.73$, suggesting that the bump would start retracting as the supersonic region extends past the location of the breather holes and the cavity pressure tends towards the freestream supersonic value. It may be expected that, when the rear leg of the λ-shock is off the bump, there would be no pressure differential across it, in the same way as for the upstream shock case, and the bump would fully retract. However, the downstream shock profile in Fig. 13 is taller than that for an upstream shock. This is explained by the fact that, while for high cavity pressures the mass flow rate through the breather holes is much larger than the leakage mass flow so $P_c \approx P_{freestream}$ (Fig. 12(a)), for lower cavity pressures the leakage mass flow becomes significant and $P_c > P_{freestream}$ (Fig. 12(b)), meaning that the flexible surface is still deformed into the flow. However, for the case of a perfect cavity seal without any leaks, the bump would be expected to fully retract for rear leg locations downstream of the flexible region.

As mentioned in Section 2.2, Fig. 13 shows that the nominally rigid portion of the plate deforms slightly under the effect of the pressure loading as $y/L_2 \neq 0$ at $x/L_2 = 0$ and 1. While this is another limitation of the experimental setup, the fact that these deformations were consistently present in all the experiments performed gives confidence in the trends discussed in this paper.

4.2.2. Stagnation pressure loss

Fig. 14 shows a plot of P_0/P_e as a function of normalised rear leg position. It includes the profiles for the cases with active control of cavity pressure (which can also be found in Fig. 10) and for the flexible plate with breather holes (in red). Recalling that P_0/P_e is an indication of overall stagnation pressure losses, Fig. 14 suggests that the presence of the passively controlled bump does not have a very significant impact on losses relative to the baseline solid flat plate case.

The main reason for this is the limited height of the deployed bump, which restricts how much it can affect the flow, especially given its three-dimensionality (Bruce and Colliss, 2015). Compared with the plots in Fig. 9, the passive bump is shorter than the actively controlled bump with a constant cavity pressure of $P_c/P_0 = 0.61$ ($(y/L_2)_{max} = 0.008$ compared to 0.013), and this is consistent with the relative position of the curves in Fig. 14.

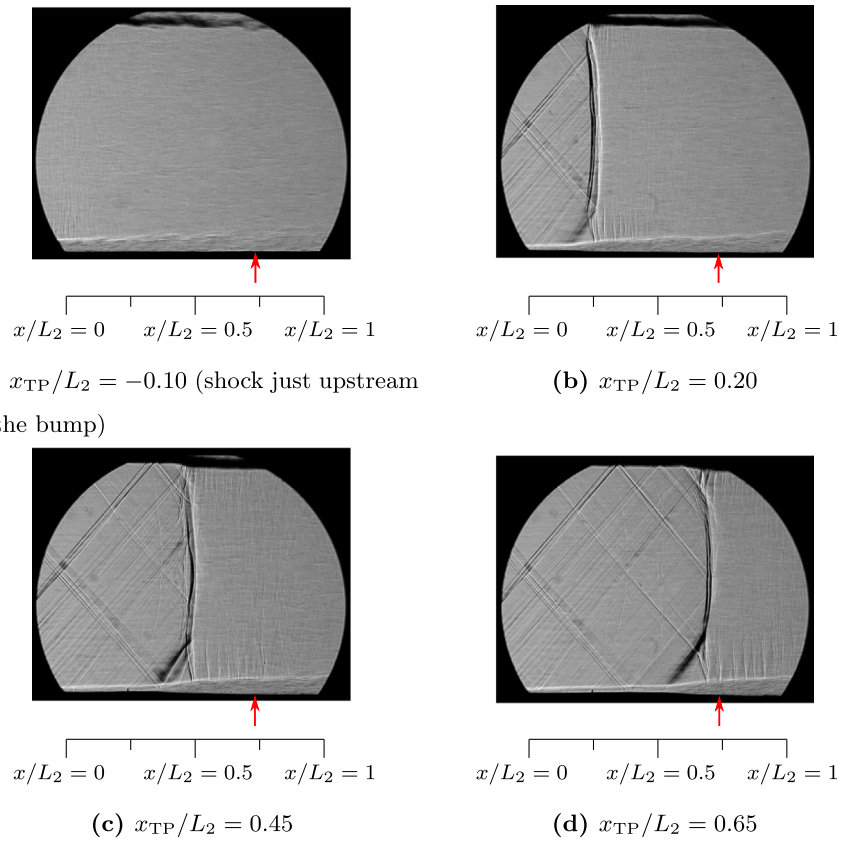

Fig. 15. Schlieren images showing the shock structure above the flexible plate for four different triple point positions. The red arrows indicate the streamwise location of the breather holes. $M = 1.4$, $P_0 \approx 130$ kPa.

4.2.3. 3D results

Despite the models tested being 3D, the focus of this paper has been on the centreline properties (e.g. pressure and displacement) for ease of comparison between different test cases. This section complements the rest of the paper by presenting the 3D plate shape and pressure field above the passive adaptive SCB for four representative triple point positions ($x_{TP}/L_2 = -0.10, 0.20, 0.45, 0.65$). The schlieren images in Fig. 15 show the shock structure above the flexible surface for the different cases and Fig. 16 the corresponding plate shapes. As already seen in Fig. 13, the bump becomes taller as the shock moves downstream due to the increase in pressure differential across it.

Frame rate. Before presenting the 3D pressure distributions, a comment should be made about the choice of frame rate. As mentioned in Section 3, videos were recorded at 100 Hz to capture the dynamics associated with the oscillating λ-shock structure. The interframe time (and therefore maximum exposure time allowed) of 9.9 ms is significantly lower than the quoted PSP response time of 750 ms (Table 3). However, it is known that, provided that the timescale of oxygen diffusion through the polymer binder is significantly larger than the luminescent lifetime of the paint (which is often the case), the PSP time response is controlled by oxygen diffusion and is therefore proportional to the square of the paint thickness (Liu et al., 2001). For this reason, a thin layer of paint was applied over the base coat. To support this choice of frame rate, the shock position detected from pressure tappings, PSP and schlieren over one second of a test is compared in Fig. 17. The agreement between the three profiles in Fig. 17 confirms that the selected paint could properly detect the unsteady normal shock. This gives confidence in the accuracy of the pressure distribution measured everywhere on the plate.

Pressure distribution. The 3D pressure distributions for the four triple point positions (obtained from PSP) can be found in Fig. 18. The PSP results were averaged over 10 pixels between $z/L_2 = -0.02$ and -0.04 to obtain representative centreline profiles. Fig. 19 shows the comparison between centreline results obtained from pressure tappings and PSP (in grey). The good agreement between the two sets of results gives further confidence in the accuracy of the PSP technique, including the use of temperature-dependent calibration coefficients discussed in Section 3.3 and the choice of exposure time.

Fig. 18 reveals a highly-3D pressure distribution on the bump, in particular at the leading edge, where the strength of the front leg changes across the span as the surface curvature decreases from the centreline towards the sides of the wind tunnel. This effect is particularly evident in Figs. 18(c) and 18(d), as the taller bump leads to a stronger oblique shock along

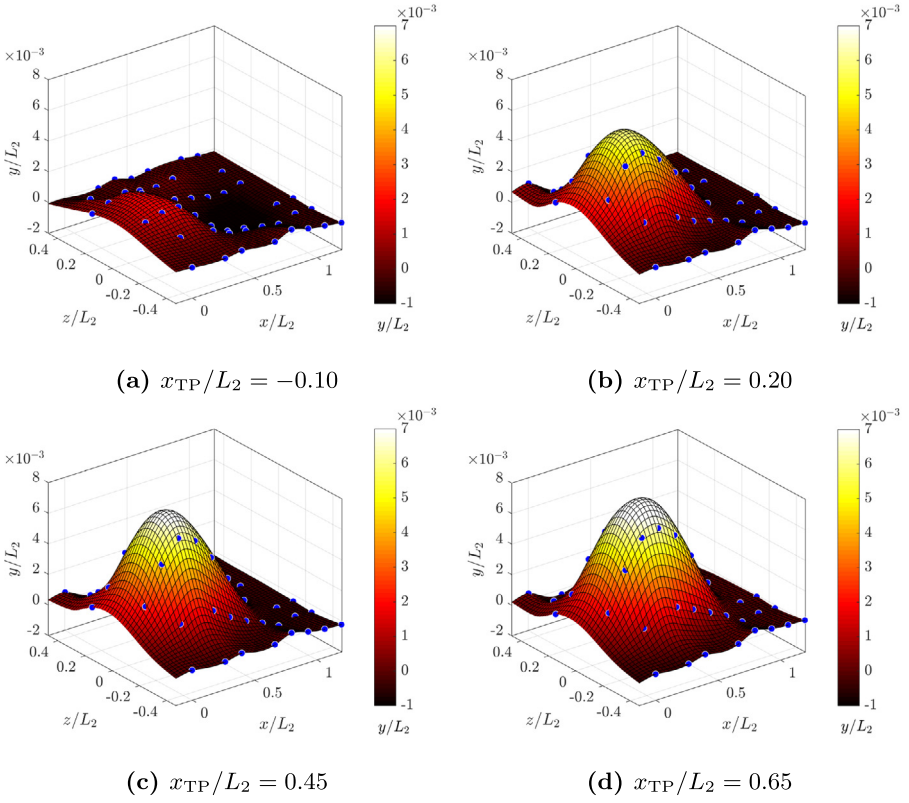

Fig. 16. Bump shapes for four different triple point positions. $M = 1.4$, $P_0 \approx 130$ kPa.

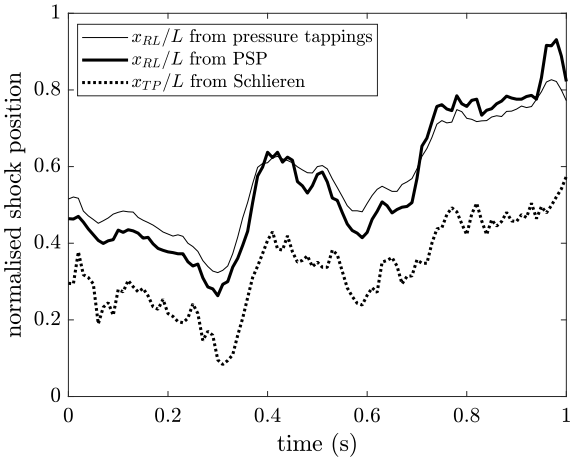

Fig. 17. Comparison between normalised shock position obtained from pressure tappings, PSP and schlieren. $M = 1.4$, $P_0 \approx 130$ kPa.

the centreline, which amplifies differences across the span. These differences in shock angle and strength justify why the front leg is not very sharp in the schlieren images (Fig. 15): schlieren provides a spanwise average, and the flow features appear more faint (compared with 2D equivalents) in the case of spanwise non-uniformities. After the pressure rise associated with the front leg, Figs. 18(c) and 18(d) show some supersonic re-acceleration due to the surface curvature, followed by the final pressure rise caused by the rear leg. This bifurcated structure is not observed in Figs. 18(a) and 18(b) as, for the former, the shock is upstream of the bump, and, for the latter, coalescence of the normal shock and front leg mean that the flexible plate only experiences one pressure rise. This can be seen clearly from the centreline profiles in Fig. 19.

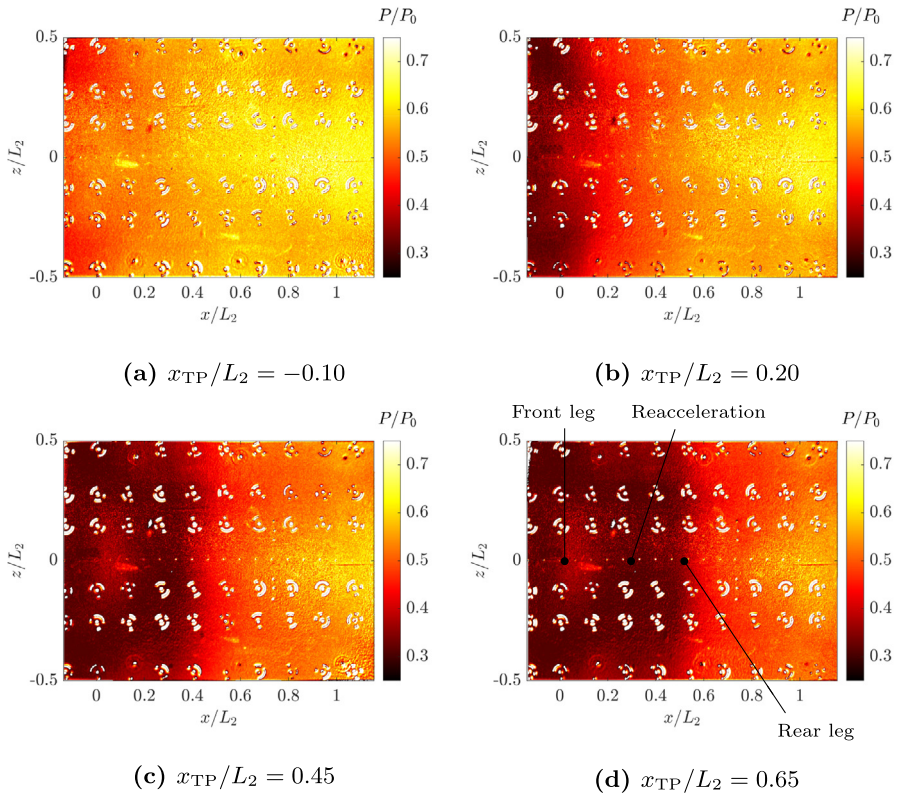

Fig. 18. 3D pressure field for four different triple point positions. $M = 1.4$, $P_0 \approx 130$ kPa.

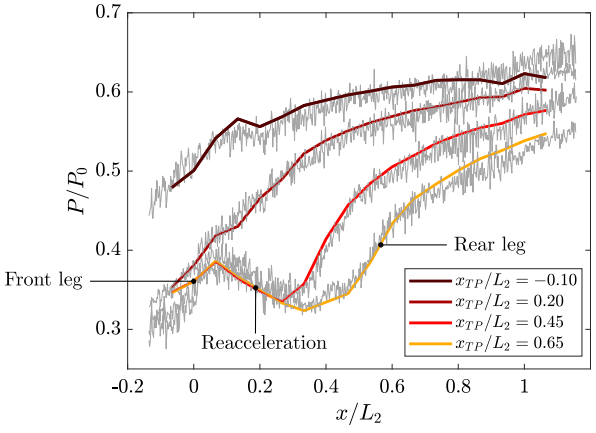

Fig. 19. Comparison between the centreline pressure distribution from pressure tappings and pressure sensitive paint. The PSP results, averaged between $z/L_2 = -0.02$ and -0.04, are plotted in grey. $M = 1.4$, $P_0 \approx 130$ kPa.

Figs. 18 and 19 also show that the small airflow through the breather holes does not affect the global flowfield as no discontinuities are observed in the pressure distribution around the location of the breather holes ($x/L_2 = 0.73$). This is in agreement with the schlieren images in Fig. 15, where no unusual flow features can be observed.

5. Conclusions

The response of a 3D flexible plate to shock impingement with active (using a manually-operated valve) and passive (through breather holes) control of cavity pressure has been studied through wind tunnel experiments with a Mach 2 oblique shock and a Mach 1.4 normal shock in an effort to improve the off-design performance of adaptive SCBs.

Experiments with active control of cavity pressure have shown that the aerostructural behaviour of the flexible plate is a strong function of the pressure in the cavity and of shock position. A reduction in stagnation pressure losses associated

with the shock structure was observed during tests with the highest cavity pressures, when the plate assumed the shape of a 3D SCB. With appropriately sized and located breather holes, the bump deployed when the shock was on the flexible surface, and remained flat otherwise. This result is highly promising, as it shows significant potential for reducing the off-design performance of SCBs. Greater surface deformations and reduced stagnation pressure losses could be obtained by using a material with lower bending stiffness (but reasonably high membrane stiffness), tailored compliance, or by applying the same actuation mechanism to 2D adaptive SCBs.

Capabilities were developed to take simultaneous pressure sensitive paint and photogrammetry measurements and results showed that it is possible to generate an accurate reconstruction of the 3D pressure field above a deforming flexible surface.

CRediT authorship contribution statement

Michela Gramola: Writing – original draft, Conceptualization, Investigation, Methodology. **Paul J.K. Bruce:** Supervision, Writing – review & editing, Conceptualization, Methodology. **Matthew Santer:** Supervision, Writing – review & editing, Conceptualization, Methodology.

Declaration of competing interest

The authors declare that they have no known competing financial interests or personal relationships that could have appeared to influence the work reported in this paper.

Acknowledgements

The first author wishes to acknowledge the Imperial College London President's PhD Scholarship Scheme, supported by EPSRC, UK, for their support of this research.

Appendix

In the absence of viscosity, it would not be possible to hold a normal shock at a given location in a parallel duct by controlling the stagnation pressure ratio across it. On the plot of P_0/P_e against shock position in Fig. 20, this (ideal) case

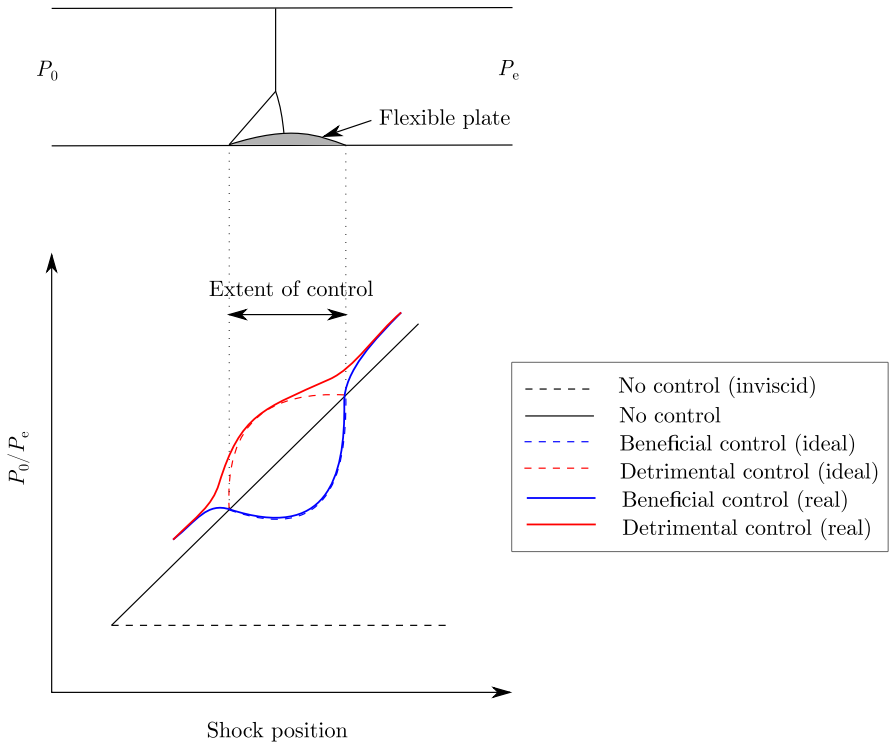

Fig. 20. Schematic diagram showing the stability of a normal shock in the working section of a blow down supersonic wind tunnel with and without a flexible plate. (For interpretation of the references to colour in this figure legend, the reader is referred to the web version of this article.)

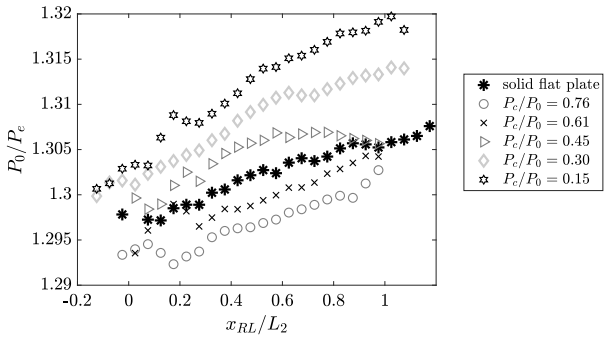

(a) Rear leg

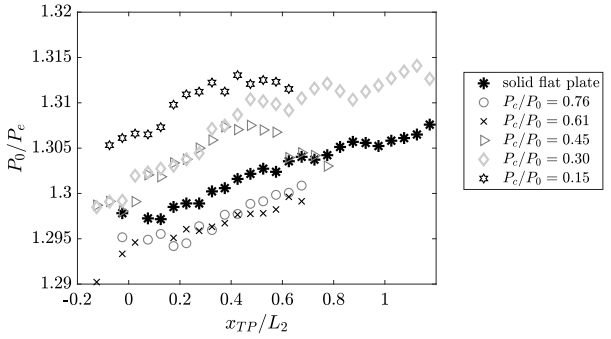

(b) Triple point

Fig. 21. Plots of stagnation pressure ratio as a function of rear leg and triple point position for the flexible plate with different cavity pressures and the baseline case of a solid flat plate. $M = 1.4$.

is represented by the dashed black line, which has zero gradient. However, when viscosity is considered, a relationship can be determined between shock position and stagnation pressure ratio by balancing the overall losses within the duct.

Considering the case of a normal shock wave in a parallel duct with boundary layers on the top and bottom walls, the difference between inlet and outlet stagnation pressures ($\Delta P_0 = P_0 - P_e$) must be equal to the total losses within the duct, which are composed of viscous losses in the boundary layer and stagnation pressure losses across the shock wave. Assuming small boundary layer growth, the normal shock strength can be considered independent of shock position, and so is the stagnation pressure drop across it. Therefore, any variation in ΔP_0 must be accommodated by a change in viscous losses within the boundary layer, which are affected by shock position (as they are higher in the pre-shock boundary layer). This implies that, as ΔP_0 increases, the normal shock stabilises at a more downstream streamwise location, such that the greater viscous losses compensate for the increase in ΔP_0. This gives rise to an approximately linear relationship between stagnation pressure ratio and shock position, as indicated by the solid black line in Fig. 20.

It should be noted that in this analysis any change in stagnation pressure losses due to friction in the diffuser between the different shock positions is assumed to be small relative to the losses in the working section. In fact, an order of magnitude calculation taking into account frictional losses in the working section and stagnation pressure losses across the normal shock has shown that the flow conditions at the diffuser entry are almost independent of shock position. For example, a difference in Mach number and total pressure around 1% was computed for a change in shock position of 150 mm.

The presence of a flexible plate on the bottom wall of the duct generates a more complex shock structure, and the stagnation pressure drop across it is now a function of its position relative to the flexible plate. For a given value of stagnation pressure ratio, if the flexible plate deforms into a beneficial shock control device, a stable shock will be observed at a more downstream streamwise position compared with the uncontrolled case. In fact, greater viscous losses (associated with the pre-shock boundary layer) are required to match ΔP_0 given the lower stagnation pressure losses across the shock. The opposite is true for a detrimental control device that increases the losses across the shock system. These two trends are shown by the dashed blue and red lines in Fig. 20.

While in an ideal case the presence of the deployed flexible plate only affects the stability of a shock directly above it, in practice additional stagnation pressure losses are usually experienced for shock positions upstream and downstream of the flexible plate, as its presence and effect on the overall flowfield cannot be neglected. This is indicated by the solid blue and red lines in Fig. 20.

An additional comment should be made about the definition of shock position above a deflected flexible plate, which generates a bifurcated shock structure (as shown in Fig. 5). While comparing triple point positions (for a given value of normalised stagnation pressure) across different test cases may be regarded as a more rigorous way to take into account the balance of overall losses associated with the deformed flexible plates (skin friction in the boundary layer and entropy generation across the shock structure), the detection of rear leg position is more consistent across the different test cases, hence both results are reported in Fig. 21. Statistical binning of the instantaneous data is employed to calculate representative mean values with bin size $\Delta(x_{RL}/L_2) = \Delta(x_{TP}/L_2) = 0.05$. The very good agreement between the trends in Figs. 21(a) and 21(b) confirms that either triple point or rear leg can be used to compare the losses associated with the flexible plates with different cavity pressures. Results are presented in this paper as a function of rear leg position.

References

Babinsky, H., Harvey, J.K., 2011. Shock Wave-Boundary-Layer Interactions, Vol. 32. Cambridge University Press.

Beberniss, T., Eason, T., Spottswood, S., 2012. High-speed 3D digital image correlation measurements of long-duration random vibration; recent advancements and noted limitations. In: Proceedings of International Conference on Noise and Vibration Engineering (ISMA). Katholieke Universiteit Leuven, Belgium.

Bruce, P.J.K., Colliss, S.P., 2015. Review of research into shock control bumps. Shock Waves 25 (5), 451–471.

Dargel, G., Thiede, P., 2002. Assessment of shock and boundary layer control concepts for Hybrid Laminar Flow wing design. In: Drag Reduction by Shock and Boundary Layer Control. Springer, pp. 383–414.

Daub, D., Willems, S., Gülhan, A., 2015. Experiments on the interaction of a fast-moving shock with an elastic panel. AIAA J. 54 (2), 670–678.

Gramola, M., Bruce, P.J.K., Santer, M., 2018. Experimental FSI study of adaptive shock control bumps. J. Fluids Struct. 81, 361–377.

Gramola, M., Bruce, P.J.K., Santer, M., 2019. Photogrammetry for accurate model deformation measurement in a supersonic wind tunnel. Exp. Fluids 60 (1), 8.

Gramola, M., Bruce, P.J.K., Santer, M., 2020. Off-design performance of 2D adaptive shock control bumps. J. Fluids Struct. 93, 102856.

Gramola, M., Bruce, P.J.K., Santer, M., 2021. Temperature corrected pressure sensitive paint measurements on a flexible surface. In: AIAA Scitech 2021 Forum. p. 0128.

Innovative Scientific Solution Incorporated, 2019. Single-component pressure sensitive paint. URL: https://psp-tsp.com/products/304/single-component-pressure-sensitive-paints.html.

Jinks, E., Bruce, P.J.K., Santer, M., 2018. Optimisation of adaptive shock control bumps with structural constraints. Aerosp. Sci. Technol. 77, 332–343.

Jones, N.R., Jarrett, J.P., 2018. Designing a shock control bump array for a transonic wing–body model. AIAA J. 56 (12), 4801–4814.

Liu, T., Teduka, N., Kameda, M., Asai, K., 2001. Diffusion timescale of porous pressure-sensitive paint. AIAA J. 39 (12), 2400–2402.

Meier, H.U., 1977. Measuring techniques for compressible turbulent boundary layers. In: NASA STI/Recon Technical Report N 79. p. 16240.

Nübler, K., Lutz, T., Kraemer, E., Colliss, S., Babinsky, H., 2012. Shock control bump robustness enhancement. In: 50th AIAA Aerospace Sciences Meeting Including the New Horizons Forum and Aerospace Exposition. p. 46.

Peltier, S.J., Rice, B.E., Szmodis, J., Ogg, D.R., Hofferth, J.W., Sellers, M.E., Harris, A.J., 2019. Aerodynamic response to a compliant panel in Mach 4 flow. In: AIAA Aviation 2019 Forum. p. 3541.

PhotoModeler, 2018. User guide. URL: https://www.photomodeler.com.

Ravichandran, R., Gramola, M., Bruce, P.J.K., 2020. Simultaneous pressure and displacement measurements on a 3D flexible surface in a supersonic flow. In: AIAA Scitech 2020 Forum. p. 0315.

Rhodes, O., Santer, M., 2011. Structural optimization of a morphing shock control bump. In: The Proceedings of 52nd AIAA/ASME/ASCE/AHS/ASC Strutures, Strutural Dynamics and Materials Conference, Denver, Colorado. pp. 2129–2147.

Spottswood, S.M., Beberniss, T.J., Eason, T.G., Perez, R.A., Donbar, J.M., Ehrhardt, D.A., Riley, Z.B., 2019. Exploring the response of a thin, flexible panel to shock-turbulent boundary-layer interactions. J. Sound Vib. 443, 74–89.

Stanewsky, E., Délery, J., Fulker, J., de Matteis, P., 2002. Synopsis of the project EUROSHOCK II. In: Drag Reduction by Shock and Boundary Layer Control. Springer, pp. 1–124.

Threadgill, J.A., Bruce, P.J.K., 2015. Unsteadiness in shock wave boundary layer interactions across multiple interaction configurations. In: 53rd AIAA Aerospace Sciences Meeting. p. 1977.

Threadgill, J.A., Bruce, P.J., 2020. Unsteady flow features across different shock/boundary-layer interaction configurations. AIAA J. 1–13.

Visbal, M., 2014. Viscous and inviscid interactions of an oblique shock with a flexible panel. J. Fluids Struct. 48, 27–45.